Optimized Diffusion-Weighting Gradient Waveform Design (ODGD) Formulation for Motion Compensation and Concomitant Gradient Nulling

Authors:

Óscar Peña-Nogales[1†], Yuxin Zhang[2,3†], Xiaoke Wang[3,4], Rodrigo de Luis-Garcia[1], Santiago Aja-Fernández[1], James H. Holmes[3] and Diego Hernando[2,3]

[1]Laboratorio de Procesado de Imagen, Universidad de Valladolid, Valladolid, Spain

Departments of [2]Medical Physics, [3]Radiology, and [4]Biomedical Engineering, University of Wisconsin-Madison, Madison, WI, United States

Corresponding Author:

Diego Hernando, PhD

Wisconsin Institutes for Medical Research

University of Wisconsin-Madison

1111 Highland Ave

Madison, WI 53705

dhernando@wisc.edu

Phone: 608-265-7590

Keywords: Diffusion-weighted imaging (DWI), diffusion-weighting gradient waveforms, optimization, motion compensation, concomitant gradient (CG)-nulling

Abstract Word count: 200

Word count: XXX

[†]These authors contributed equally to this work

ABSTRACT

Purpose: To present a novel Optimized Diffusion-weighting Gradient waveform Design (ODGD) method for the design of minimum echo time (TE), bulk motion-compensated, and concomitant gradient (CG)-nulling waveforms for diffusion MRI.

Methods: ODGD motion-compensated waveforms were designed for various moment-nullings M_n (n=0,1,2), for a range of b-values, and spatial resolutions, both without (ODGD-M_n) and with CG-nulling (ODGD-M_n-CG). Phantom and in-vivo (brain and liver) experiments were conducted with various ODGD waveforms to compare motion robustness, signal-to-noise ratio (SNR), and apparent diffusion coefficient (ADC) maps with state-of-the-art waveforms.

Results: ODGD-M_n and ODGD-M_n-CG waveforms reduced the TE of state-of-the-art waveforms. This TE reduction resulted in significantly higher SNR ($P < 0.05$) in both phantom and in-vivo experiments. ODGD-M_1 improved the SNR of BIPOLAR (42.8±5.3 versus 32.9±3.3) in the brain, and ODGD-M_2 the SNR of motion-compensated (MOCO) and Convex Optimized Diffusion Encoding-M_2 (CODE-M_2) (12.3±3.6 versus 9.7±2.9 and 10.2±3.4, respectively) in the liver. Further, ODGD-M_2 also showed excellent motion robustness in the liver. ODGD-M_n-CG waveforms reduced the CG-related dephasing effects of non CG-nulling waveforms in phantom and in-vivo experiments, resulting in accurate ADC maps.

Conclusions: ODGD waveforms enable motion-robust diffusion MRI with reduced TEs, increased SNR, and reduced ADC bias compared to state-of-the-art waveforms in theoretical results, simulations, phantoms and in-vivo experiments.

Keywords: Diffusion-weighted imaging (DWI), diffusion-weighting gradient waveforms, optimization, motion compensation, concomitant gradient (CG)-nulling

INTRODUCTION

Diffusion-weighted (DW) MRI has a unique ability to non-invasively probe tissue microstructure (1, 2). By applying powerful diffusion-weighting gradient waveforms (3), DW-MRI is sensitive to the microscopic Brownian motion of water molecules, with multiple applications for tissue characterization in health and disease (4, 5).

However, the application of these powerful diffusion-weighting gradients results in significant imaging challenges, including signal dephasing due to bulk motion (1, 6, 7) as well as due to concomitant gradients (CGs) (8–10). Bulk motion artifacts are particularly severe in organs that experience substantial physiological motion (e.g., heart and liver). In these organs, the presence of macroscopic elastic tissue motion during the application of the diffusion gradients can result in localized signal voids (11–14). CGs are inherent to any diffusion-weighting gradient waveform due to the constraints imposed by Maxwell's equations, and can introduce large spatially dependent dephasing in diffusion MRI sequences where the diffusion gradients are not symmetric about the refocusing radiofrequency pulse (9). Bulk motion- and CG-related signal dephasing can complicate the interpretation of DW images and introduce bias and variability in the quantification of diffusion parameters.

Multiple approaches have been proposed to address the effects of bulk motion and CGs in several MRI applications. These approaches include both acquisition-based and reconstruction-based methods, as described next:

- Bulk motion artifacts can be reduced through the synchronization of the DW acquisition (1). Synchronizing the DWI acquisition with the bulk physiological motion (e.g., using cardiac and/or respiratory triggering) reduces motion artifacts, although these methods generally increase the overall acquisition time (6). Further, elastic motion can occur regionally throughout the entire cardiac or respiratory cycle, therefore triggered acquisitions are generally not able to completely avoid motion artifacts. Sensitivity to bulk motion can be further reduced by applying diffusion-weighting gradient waveforms that guarantee first- and/or second-order moment-nulling (15–17). Traditionally, first-order moment-nulling (i.e., velocity compensation) has been achieved with bipolar waveforms (16), and second-order moment-nulling (i.e., acceleration compensation) with 'motion-compensated' diffusion encoding gradient waveforms (17). However, first- and second-order moment-nulled diffusion waveforms have typically resulted in substantial increases in the achievable echo times (TEs), leading to low signal-to-noise ratio

(SNR) efficiency in these acquisitions.

- CG-effects can be minimized using multiple different approaches, including: postprocessing-based methods (18), shimming coils (19), image gradients dephasing (9), and application of symmetric diffusion-weighting gradient waveforms such as monopolar gradients (20), or waveform reshaping to guarantee phase cancellation (10).

Recently, Aliotta et al. (21) proposed a novel algorithm, termed Convex Optimized Diffusion Encoding (CODE), to design gradient waveforms with first- and/or second-order moment-nulling. By formulating the gradient waveform design problem as a constrained nonlinear optimization problem (with constraints including sequence timing, hardware limits, and moment-nulling), CODE enables flexible design of gradient waveforms and seeks to minimize the achievable TE for a desired b-value (or conversely, to maximize the achievable b-value for a given TE). By approximating this constrained optimization formulation as a convex (linear) optimization problem (instead of the original nonlinear, non-convex quadratic problem), CODE results in simplified computation. However, because of this approximation, it is unclear whether CODE results in optimal waveforms, i.e., whether it achieves the minimum TE for a given desired b-value. This optimality is critical for moment-nulled diffusion-weighting waveform design, as it will determine the signal-to-noise ratio (SNR) of the DWI acquisition, particularly for organs with relatively short T_2 relaxation time (e.g., the liver). Further, CODE waveforms are generally asymmetric around the refocusing pulse, therefore they suffer from substantial CG-effects, which need to be addressed. Although the CODE-designed diffusion-weighting gradient waveforms can be subsequently modified to reduce CG-effects (21), it is unclear how this subsequent modification affects the overall optimality of the waveform.

Therefore, in this study we propose a novel Optimized Diffusion-weighting Gradient waveform Design (ODGD) method for diffusion-weighting gradient waveform design that seeks to overcome the limitations of previous methods. The proposed ODGD method consists of: 1) a constrainted optimization formulation that minimizes the TE for a given b-value subject to moment-nulling and CG-nulling constraints, and 2) a quadratic optimization algorithm that directly solves the formulation without introducing approximations. In this manuscript, the proposed method is described and evaluated in phantoms and in-vivo brain and liver diffusion MRI experiments.

THEORY

The proposed Optimized Diffusion-weighting Gradient waveform Design (ODGD) formulation seeks to optimize the TE for a given b-value, under various linear and nonlinear constraints. These constraints are listed below.

Moments

In order to refocus the signal from static spins, all diffusion-weighting gradient waveforms require zeroth-order moment-nulling (M_0). Additionally, diffusion-weighting gradient waveforms with high-order moment-nulling are desirable in tissues affected by physiological motion in order to avoid motion-related signal dephasing (importantly, this dephasing will result in artifactual signal decay in voxels that experience elastic tissue motion). These moment constraints can be expressed as follows (22):

$$M_{\mathrm{n}} = \gamma \int_0^{T_{\mathrm{Diff}}} t^{\mathrm{n}} G(t) dt = 0 \quad \text{where} \quad \mathrm{n} = 0, 1, 2... \qquad [1]$$

where γ is the gyromagnetic ratio, and G(t) and T_{Diff} are the diffusion-weighting waveform and the diffusion-weighting time, respectively. Under this constraint, $M_0 = 0$ rephases the static spins, $M_1 = 0$ rephases the spins moving with uniform speed, and $M_2 = 0$ rephases the spins moving with uniform acceleration. In the present work:

- ODGD-M_0 stands for ODGD with $M_0 = 0$.
- ODGD-M_1 stands for ODGD with $M_0 = M_1 = 0$.
- ODGD-M_2 stands for ODGD with $M_0 = M_1 = M_2 = 0$.

Concomitant Gradients

Concomitant Gradients (CGs) are well-known nonlinear spatially dependent magnetic fields that appear, as a consequence of Maxwell's equations for the curl and divergence, anytime we generate a magnetic field gradient (8). In conventional MRI scanners (8, 10), these CGs are orthogonal to the diffusion-weighting gradients, and have significant first- and second-order spatially varying terms as follows:

$$B_c(x, y, z, t) = \frac{1}{2B_0}[(G_x^2(t) + G_y^2(t))z^2 + G_z^2(t)\frac{x^2 + y^2}{4} - G_x(t)G_z(t)xz - G_y(t)G_z(t)yz] \qquad [2]$$

where B_c is the CG magnetic field, B_0 is the amplitude of the static magnetic field, and $G_x(t)$, $G_y(t)$, and $G_z(t)$ are the diffusion-weighting gradients applied in the x, y, and z directions, respectively. Importantly, CGs are small near isocenter, and increase in magnitude away from isocenter. These nonlinear and spatially dependent magnetic fields can cause a phase accrual throughout the gradient diffusion-weighting time (T_{Diff}) given by:

$$\phi_c(x,y,z) = \gamma \int_0^{T_{\mathrm{Diff}}} B_c(x,y,z,t)dt \quad [3]$$

Therefore, the application of gradients leads to a spatially dependent dephasing of the MRI signal. This dephasing may cause a blurring of the k-space due to parabolic phase variations within the imaging plane, and a shifting of the k-space due to the cross-terms G_iG_j, so called in-plane dephasing (9). In addition, through-plane phase dispersion resulting from CGs (9) may cause severe signal attenuation. Further, this additional signal decay will be larger for increasing b-values, which may introduce bias in quantitative diffusion measures.

Consequently, in order to address the effects of CGs, the CG-related phase accrual can be nulled by incorporating the following nonlinear constraint into the diffusion-weighting gradient waveform design formulation:

$$\phi_c(x,y,z) = 0 \quad [4]$$

By including this constraint, CG artifacts will be avoided by design.

Additional Constraints

Diffusion-weighted MRI sequences need to satisfy additional hardware constraints such as the limitation on the maximum gradient intensity (G_{Max}) and maximum slew rate (SR_{Max}). Further, diffusion-weighting gradient waveforms need to be zero at certain times during the pulse sequence (e.g., during the RF pulses). In this work, we will only focus on the constraints imposed by the spin-echo DWI sequence (21):

$$G(\mathrm{RF}_{90}) = 0 \quad [5]$$

$$G(\mathrm{RF}_{180}) = 0 \quad [6]$$

$$G(\mathrm{T}_{\mathrm{EPI}}) = 0 \quad [7]$$

$$G(t) \leq \mathrm{G_{Max}} \quad [8]$$

$$\dot{G}(t) \leq \mathrm{SR_{Max}} \quad [9]$$

where $\mathrm{RF_{90}}$ corresponds to the excitation pulse and $\mathrm{RF_{180}}$ corresponds to the refocusing pulse. $\mathrm{T_{EPI}}$ is the time needed by the EPI echo train to reach the center of k-space. In summary, the diffusion-weighting waveform may begin immediately after the excitation pulse, is zero during the refocusing pulse, and needs to finish before the beginning of the EPI echo train.

Proposed Formulation

The proposed ODGD formulation seeks to maximize the achievable b-value for a given TE. The b-value is given by

$$b = \gamma^2 \int_0^{T_{\mathrm{Diff}}} F(t)^2 dt \quad [10]$$

where

$$F(t) = \int_0^t G(\tau) d\tau \quad [11]$$

Therefore, the maximization is performed directly over the b-value formulation (without the approximations introduced in previous works (21)), by optimizing the diffusion-weighting gradient waveform subject to the constraints in Eqs. [1-9]. Hence, the objective function is formulated as follows:

$$G(t) = \arg\max_{G} b(G) \quad [12]$$

For sake of clarity, Table 1 summarizes the constraints of the ODGD formulation. Importantly, it is generally of interest to minimize the TE for a given b-value (rather than to maximize the b-value for a given TE). To achieve the minimum TE for a given b-value, ODGD iteratively implements the maximization described in Eq. [12] at several TEs following a similar solution strategy as described in Figure 2 of (21).

Optimization Algorithm

In this work, Eq. [12] is directly solved using a sequential quadratic programming (SQP) algorithm subject to upper and lower bounds (Eq. [8]), linear equality constraints (Eqs. [1] and [5 - 7]), linear inequality constraints (Eq. [9]), and a quadratic equality constraint (Eq. [4]). This optimization is performed in MATLAB (MathWorks, Natick, MA) using the *fmincon* built-in function.

METHODS

Optimized Diffusion-weighting Gradient Waveform Design

The performance of the proposed ODGD method and previous waveform designs were compared by assessing the TE needed to achieve a given b-value for each waveform. Specifically, gradient waveforms were compared for a broad range of b-values (100 - 2000 s/mm^2). Additionally, because the achievable TE also depends on the time needed by the EPI echo train to reach the center of k-space (which will itself depend on the desired spatial resolution and degree of partial Fourier acquisition), different EPI readout times to the center of k-space (T_{EPI} = 15 - 50 ms) were considered for each b-value. Diffusion-weighting gradient waveforms were designed using the following hardware and time constraints: excitation radiofrequency pulse duration of RF_{90} = 5.3 ms; refocusing pulse duration of RF_{180} = 4.3 ms; maximum gradient strength of G_{Max} = 49 mT/m; maximum slew rate of SR_{Max} = 100 T/m/s; unless otherwise stated, only one gradient direction was considered for the computation of the b-values (note that CG-effects will depend on the diffusion-weighting direction). All waveform designs were computed with a time resolution of 0.5 ms to optimize the waveforms in moderate computation times.

For each T_{EPI} and b-value, the following gradient waveforms were designed: 1) monopolar (MONO) (20), 2) bipolar (BIPOLAR) (16), 3) motion-compensated (MOCO) diffusion-encoding gradient waveforms (17), 4) three Convex Optimized Diffusion Encoding (21) waveforms, one for each of the motion-nulling moments (CODE-M_n, where n=0,1,2), and 5) the proposed ODGD formulation for each of the motion-nulling moments (ODGD-M_n, where n=0,1,2) without and with CG-nulling (ODGD-M_n-CG, where n=0,1,2). In this study, the optimization algorithm for ODGD-M_n waveforms was initialized with a constant waveform, and the optimization of ODGD-M_n-CG waveforms was initialized with the corresponding ODGD-M_n waveform. Figure 1 shows examples of each of the waveforms designed for the experiments grouped as traditional designs, CODE waveforms, and ODGD waveforms without and with CG-nulling.

Evaluation of SNR Increase

Acetone phantom experiments

A ten-vial acetone-based diffusion phantom was constructed using mixtures of pure acetone (as a signal source), H_2O (to control the ADC of acetone without producing MR signal), and $MnCl_2$ (to control the T_2 of acetone) (23). The total volume of mixture in each vial was of 50 ml. The ten

vials were designed to form two T_2 groups of approximately 40 and 90 ms, respectively, with five different ADC values each. Specific vial compositions and expected approximate ADC values (23) included 1) 11.02 and 2) 4.78 mM of $MnCl_2$ with a 30% v/v of H_2O for ADC = 0.9×10^{-3} mm^2/s, 3) 13.89 and 4) 6.03 mM of $MnCl_2$ with a 20% v/v of H_2O for ADC = 1.2×10^{-3} mm^2/s, 5) 15.94 and 6) 6.92 mM of $MnCl_2$ with a 15% v/v of H_2O for ADC = 1.5×10^{-3} mm^2/s, 7) 17.50 and 8) 7.60 mM of $MnCl_2$ with a 12% v/v of H_2O for ADC = 1.8×10^{-3} mm^2/s, and 9) 19.38 and 10) 8.42 mM of $MnCl_2$ with a 9% v/v of H_2O for ADC = 2.1×10^{-3} mm^2/s, where the number before the $MnCl_2$ concentration represents the vial number.

Diffusion-weighted images of the diffusion phantom were acquired under 0°C ice-water bath with an eight-channel head coil in a 3T scanner (MR 750, GE Healthcare, Waukesha, WI). The specific constraints of the optimization formulation are T_{EPI} = 23 ms, RF_{90} = 5.5 ms, RF_{180} = 6 ms, G_{Max} = 49 mT/m and SR_{Max} = 100 T/m/s. Twelve different diffusion-weighting gradient waveforms with these constraints were designed with MONO, BIPOLAR, MOCO, CODE-M_n (n=0,1,2), ODGD-M_n (n=0,1,2) and ODGD-M_n-CG (n=0,1,2), respectively. Axial images were acquired using different waveforms with FOV = 26 × 26 cm, in-plane resolution = 2.0 × 2.0 mm, slice thickness = 5 mm, TR = 6 s, parallel imaging acceleration of 2 and no partial-Fourier acquisitions. Diffusion encoding was performed in all three orthogonal directions with b-values = [100(1), 400(1), 600(2), 800(4), 1000(6)] s/mm^2, where the number in brackets represents the number of averages for each b-value.

In order to perform T_2 mapping, spin-echo images were acquired with FOV = 26 × 15.6 cm, matrix size of 256 x 160, slice thickness of 10 mm, TR = 2 s, parallel imaging acceleration factor of 2, and TE = [6, 20, 60, 120, 240] ms. T_2 maps were estimated with least squares fitting.

In order to compare SNR across different acquisitions, SNR maps were calculated for each acquisition using a Rician non-stationary noise model (24), with spatially-varying noise standard deviation $\sigma(\boldsymbol{x})$. SNR maps were computed from the averaged composite magnitude images (e.g., complex images from different coils merged into one single magnitude image) using a Rician expectation–maximization estimator (25, 26):

$$\mathrm{SNR}(\boldsymbol{x}) = \frac{\widehat{A(\boldsymbol{x})}}{\widehat{\sigma(\boldsymbol{x})}}, \qquad [13]$$

where $\widehat{A(\boldsymbol{x})}$ and $\widehat{\sigma(\boldsymbol{x})}$ are the estimates of the signal amplitude and noise standard deviation, respectively, obtained from an iterative process (26). Local parameters were estimated using 3 × 3 windows and a total of 20 iterations. For evaluation of SNR, a 0.9 cm^2 ROI was drawn in each vial, co-localized across the different acquisitions.

In-vivo acquisitions

This HIPAA-compliant study including healthy volunteers was performed with institutional review board approval and informed written consent.

Brain DWI Ten healthy volunteers were recruited for brain DWI. Brain DWI was acquired with the same waveform designs and constraints as the diffusion phantom experiment described in the previous section with the eight-channel head coil, and on the same 3T scanner. The acquisition parameters were FOV = 26 × 26 cm, in-plane resolution = 2.0 × 2.0 mm, slice thickness = 5 mm, TR = 2.5 s, parallel imaging acceleration factor = 2 and full k-space acquisitions. Diffusion encoding was performed in all three directions with b-values(averages) = [100(1), 200(1), 600(2), 800(4), 1000(6)] s/mm^2. SNR maps were calculated with Eq. [13]. For SNR analysis, four circular ROIs of size 38 - 50 mm^2 were drawn in the left and right cerebral white matter. ROIs in the images from different acquisitions were co-localized and SNR measurements within each subject were averaged prior to statistical comparison between different waveforms (see 'Statistical Analysis' section below for details).

Liver DWI Ten healthy volunteers were scanned with a 30-channel torso coil (GE Healthcare, Waukesha, WI) in the same 3T scanner for liver DWI. Slices covering the superior portion of the liver, including through the right and left lobes were acquired. Full liver coverage was not obtained due to time constraints for the acquisition. The constraints used for the waveform optimization were T_{EPI} = 18.5 ms, RF_{90} = 5.5 ms, RF_{180} = 6.5 ms, G_{Max} = 49 mT/m, and SR_{Max} = 100 T/m/s. Different diffusion-weighting gradient waveforms with these parameters were designed with MONO, MOCO, CODE-M_2, ODGD-M_2 and ODGD-M_2-CG, respectively. Axial images were acquired with respiratory triggering. Other acquisition parameters are FOV = 36 × 36 cm, in-plane resolution = 2.8 × 2.8 mm, slice thickness = 6 mm, parallel imaging factor of 2 and full k-space acquisitions. Diffusion encoding was performed in the R/L direction with b-values(averages) = [100(4), 500(10)] s/mm^2. SNR maps were calculated with Eq. [13] and ADC maps were estimated with least-squares fitting. For SNR analysis, circular ROIs of 50 - 100 mm^2 were drawn on the superior portion of the liver in segments VII and VIII of the right lobe, and segment IV of the left lobe. For each waveform, SNR measurements within each subject were averaged prior to statistical comparison between different waveforms. For motion compensation analysis, one ROI was set on segment II since it is typically severely impacted by cardiac motion and might contain signal voids

with traditional diffusion waveforms. Care was taken to avoid large vessels and blurred regions. Further, to measure liver T_2, a multi-TE multi-TR STEAM sequence (27) with voxel size of 20 $\times$ 20 $\times$ 20 mm was applied to all volunteers on the right lobe of the liver carefully avoiding large vessels.

Evaluation of CG-nulling

Simulations and phantom experiments

Water phantom simulations Simulations were performed in a synthetic water phantom with full k-space acquisition and same FOV, in-plane resolution, slice thickness, and waveform designs as the acetone phantom experiments. CG-related signal dephasing effects for different diffusion-weighting directions were simulated, including x, y, z, x-y, x-z, y-z and x-y-z to assess the through-plane dephasing effects. Further, the synthetic water phantom approximated the shape and dimensions, and ADC value (2×10^{-3} mm^2/s) of the following water phantom described next.

Water phantom A 7.5 L water phantom doped with NaCl and $NiCl_2$ (28) was imaged at room temperature with the same acquisition setup and the same waveform designs as the acetone phantom experiment to evaluate the CG correction effect. Seven diffusion-weighting directions were acquired, including x, y, z, x-y, x-z, y-z and x-y-z. Coverage in the slice (z) direction of 12 cm was applied to evaluate the slice dependent CG-effect, especially for slices that are away from the isocenter. ADC maps were estimated for each diffusion-weighting direction and each diffusion-weighting waveform with a maximum likelihood estimator (29).

In-vivo acquisitions

Brain DWI Average trace ADC maps were estimated from trace DW images from the previously described brain DW acquisitions with a maximum likelihood estimator (29). Hereinafter, the average trace ADC map and the trace DW images are denoted as ADC maps and DW images, respectively. ROIs measured within slices between 4.5 and 7 cm from isocenter (among the ROIs drawn on the previously described brain DW acquisitions) were considered to assess the effect of CG-related bias in ADC measurements. For each waveform, ADC measurements within each subject were averaged prior to statistical comparison between different waveforms.

Statistical Analysis

All ROIs of the phantom experiments were first tested for normality using the Kolmogorov-Smirnov (KS) test. Homoscedasticity across variances was then tested using the Ansari-Bardley test. If both tests yielded normality and homoscedasticity, respectively, pairwise comparisons were made between co-localized ROI acquired with different waveforms using the one-way sample t-test. From these comparisons, p-value (P) test with 0.05 confidence level was considered significant. Similarly, for each waveform of the in-vivo experiments, all ROI SNR and ADC measurements within each subject were averaged and then tested using the same analysis as in the phantom experiments.

RESULTS

ODGD Optimization

ODGD waveforms reduce or equalize the minimum TE of the traditional (MONO, BIPOLAR, and MOCO) and recently proposed waveforms (CODE-M_n, where n=0,1,2) for any given b-value, EPI readout time, and moment-nulling order. ODGD with CG-nulling constraints also results in shorter TE compared to the traditional waveforms. The relationship between previously proposed CODE versus the proposed ODGD solution depends on the specific constraints: CODE waveforms are sometimes the same as ODGD, sometimes a different local optimum resulting in a longer TE, and sometimes not even a local optimum (results not shown).

Moment Constraints ODGD-M_n, where n=0,1,2, outperforms the traditional waveforms as well as the recently proposed CODE-M_n gradient waveforms as shown in Figure 2. Figure 2.a) depicts the optimal TE for a range of b-values and T_{EPI} = 26.4 ms. Figure 2.b) shows the TE difference between CODE-M_n and ODGD-M_n waveforms for the range T_{EPI} = 15 - 50 ms. There is no TE reduction of ODGD-M_0 compared to CODE-M_0, but there is a TE reduction between 0 - 3.57% for M_1, and between 0.63 - 10.14% for M_2. Relative to the traditional waveforms, ODGD results in TE reductions between 1.91 - 17.84% compared to MONO, 9.20 - 29.22% compared to BIPOLAR, and 1.88 - 26.97% compared to MOCO.

Concomitant Gradients Constraints ODGD-M_n-CG, where n=0,1,2, reduces the TE of traditional CG-compensated waveforms (MONO, BIPOLAR, and MOCO, which cancel the CG phase accrual due to their symmetry around the RF_{180}), as illustrated in Figure 3. Figure 3.a) shows the minimum TE achieved for a given range of b-values and T_{EPI} = 26.4 ms of the traditional waveform designs and the proposed ODGD waveforms. Figure 3.b) shows the difference between the minimum TE achieved by the traditional and ODGD waveforms for the same range of b-values and T_{EPI} = 15 - 50 ms. Namely, ODGD-M_n-CG, where n=0,1,2, results in TE reductions between 0 - 4.02% compared to MONO, 7.53 - 16.74% compared to BIPOLAR, and 0.77 - 12.54% compared to MOCO.

Evaluation of SNR Increase

Acetone phantom experiments

Experimentally measured T_2 are 39.5±0.7 ms and 83.5±1.5, and measured ADC with respect to each of the T_2 and vial number are 1) 2.22±0.16 and 2) 2.28±0.02 × 10^{-3} mm^2/s, 3) 1.99±0.09 and 4) 1.94±0.02 × 10^{-3} mm^2/s, 5) 1.69±0.07 and 6) 1.69±0.02 × 10^{-3} mm^2/s, 7) 1.36±0.06 and 8) 1.35±0.01 × 10^{-3} mm^2/s, and 9) 0.84±0.06 and 10) 0.92±0.02 × 10^{-3} mm^2/s.

There is a 6% TE reduction of ODGD-M_2 over CODE-M_2 (TE: 118.5 ms and 126.5 ms, respectively), which generally increases the SNR in each of the diffusion phantom vials, as shown in Figure 4. Mean SNR for each of the vials is T_2 and ADC dependent, but there is an increase of 4%, -15%, 18%, 44%, 11% for each of the vials with T_2 = 39.5±0.7 ms (vial numbers 1, 3, 5, 7 and 9, respectively), and 29%, -4%, 25%, 17%, 8% for each of the vials with T_2 = 83.5±1.5 ms (vial numbers 2, 4, 6, 8 and 10, respectively) as shown in Figure 4.c-d). Statistical significance ($P < 0.05$) is found in every vial pairwise comparison except for vial 4) $T_2 \approx 83.5$ ms and ADC = 1.94±0.02 × 10^{-3} mm^2/s. ODGD-M_0 and ODGD-M_1 waveforms are the same as the correspondent CODE waveforms under the implemented spatial resolution (T_{EPI} = 23.32 ms), achieving no TE reduction, and therefore no SNR increase.

In-vivo acquisitions

Brain DWI Brain DWI results, including SNR and ADC measurements, are shown in Figure 5. ODGD-M_1 and ODGD-M_1-CG reduce the TE by 16.3% and 10.9% as compared with BIPOLAR (BIPOLAR: 119.5 ms, ODGD-M_1-CG: 106.5 ms, ODGD-M_1: 100.0 ms). There is no TE reduction of ODGD-M_1 compared to CODE-M_1. The TE reduction relative to BIPOLAR results in visually apparent increased signal (see Fig. 5.a)). ODGD-M_1 leads to higher SNR than BIPOLAR and ODGD-M_1-CG, $P < 1$ x 10^{-6} and $P < 0.05$, respectively. ODGD-M_1-CG also leads to higher SNR than BIPOLAR with $P < 0.005$.

Liver DWI The results from the liver acquisitions, with mean measured liver T_2 = 24.38±11.4 ms, are shown in Figures 6 and 7. ODGD-M_2 and CODE-M_2 waveforms result in ADC maps that are visually more homogeneous than MONO, suggesting higher motion robustness (see Fig. 6). ADC values on a ROI on segment II of the liver of a representative volunteer are 2.46±0.38 × 10^{-3} mm^2/s for MONO, 1.85±0.2 × 10^{-3} mm^2/s for CODE-M_2, and 1.53±0.21 × 10^{-3} mm^2/s for

ODGD-M_2.

ODGD-M_2 increases the TE by 47.7% as compared to MONO (from 65.3 to 96.5 ms). ODGD-M_2 (TE = 96.5 ms) reduces the TE by 8.5% and 6% as compared with MOCO (105.5 ms) and CODE-M_2 (102.5 ms), respectively. ODGD-M_2-CG (TE = 99 ms) reduces the TE by 6% and 3.5% as compared with MOCO and CODE-M_2. This TE reduction results in visually apparent increased diffusion-weighted signal and SNR (Fig. 7). ODGD-M_2 and ODGD-M_2-CG have significantly higher SNR than MOCO and CODE-M_2 (ODGD-M_2 = 12.3±3.6, ODGD-M_2-CG = 12.0±3.5 versus MOCO = 9.7±2.9 and CODE-M_2 = 10.2±3.4, both with $P < 0.05$). There is no statistically significant difference between the SNRs of ODGD-M_2 and ODGD-M_2-CG.

Evaluation of CG-nulling

Water phantom simulations and experiments

Figure 8 shows the in-plane CG-related dephasing effects for the x-y-z diffusion-weighting gradient direction in the water phantom experiments. ODGD-M_0 suffers from diffusion-weighting direction-dependent k-space shifting at the slice 4.5 cm from isocenter. Further, it also shows that ODGD-M_0 suffers from k-space blurring (i.e., larger full-width-half-maximum along the y direction, FWHMy) at isocenter (0 cm) and at 4.5 cm from isocenter. In contrast, MONO and ODGD-M_0-CG do not suffer from k-space shifting and their FWHMy is similar at both slice positions.

From simulations and phantom experiments, through-plane dephasing effects produced by CGs are demonstrated in Figure 9. Figure 9.b-c) show the direction-dependent patterns of ADC bias produced by the CG-effects of ODGD-M_1 waveforms in simulations and in the water phantom experiments, respectively. Importantly, BIPOLAR and ODGD-M_1-CG waveforms, both with CG-nulling, show improved homogeneity of ADC maps and tightly distributed histograms around the expected room-temperature water diffusion coefficient (nearly 2×10^{-3} mm^2/s) (30).

In-vivo acquisitions

Brain DWI ADC results from the brain acquisitions are shown in Figure 5. The ADC map of ODGD-M_1 pixelwise subtracted from the BIPOLAR ADC map shows visually positive general bias (see Fig. 5.c)). No bias is apparent in the pixelwise subtraction of ODGD-M_1-CG and BIPOLAR ADC maps. ODGD-M_1 leads to statistically significant higher ADC than BIPOLAR ($P < 0.005$) while there is no statistically significant difference between the ADC measured from ODGD-M_1-CG

versus BIPOLAR (BIPOLAR ADC = 0.71±0.02 x 10^{-3} mm^2/s, ODGD-M_1 ADC = 0.73±0.03 x 10^{-3} mm^2/s, and ODGD-M_1-CG ADC = 0.71±0.01 x 10^{-3} mm^2/s).

DISCUSSION

In this study, we presented a novel Optimized Diffusion-weighting Gradient waveform Design (ODGD) formulation, as a quadratic constrained optimization problem. The ODGD formulation allows the design of diffusion-weighting gradient waveforms to diminish bulk motion effects and null concomitant gradient (CG) effects while minimizing the TE of diffusion-weighted acquisitions. ODGD equalized or reduced the achievable TE compared to the traditional moment-nulled waveforms and the recently proposed CODE formulation. Generally, TE reductions are greater at higher b-values, k-space resolutions (i.e., longer T_{EPI}), and high-order moment-nulling.

The TE reduction achieved with ODGD for a given b-value over state-of-the-art waveforms may have potential applications in neuroimaging and body DW-MRI. This TE reduction may enable increased signal-to-noise ratio in DW-MRI by avoiding T_2-related signal losses. Moreover, optimized motion-compensated waveforms have promising applications in organs that experience substantial physiological motion, such as heart or liver, by enabling improved DW image quality and improved accuracy of quantitative diffusion parameter maps (14). Further, CG-nulling waveforms may be important for quantitative diffusion imaging in applications requiring a large anatomical coverage and when implementing partial Fourier acquisitions. In addition, ODGD-M_n waveforms may enable improved quantification of tissue diffusion and perfusion and characterization of non-Gaussian diffusion. Interestingly, improvements on multi-shot EPI (31) might be achieved by using ODGD-M_n waveforms due to the potential for reduced motion-induced phase variations across multiple shots.

It has been shown that ODGD-M_n results in equal or shorter TE than CODE-M_n for a given b-value. This TE reduction is likely due to the direct solution of the nonlinear optimization problem for gradient waveform design in ODGD, compared to the approximate linear formulation of the objective function used in (21). CG-nulling waveforms also shortened the achievable TE compared to the traditional symmetric MONO, BIPOLAR, and MOCO waveforms. This was likely achieved due to the elimination of dead times between radiofrequency pulses leading to more efficient use of the diffusion encoding time. Interestingly, the proposed CG-nulling formulation leads to novel smoothed asymmetric waveforms with the same squared area before versus after the refocusing RF pulse. The TE reduction of ODGD-M_0-CG and ODGD-M_2-CG compared to MONO and MOCO, respectively, are smaller than the TE reduction of ODGD-M_1-CG compared to BIPOLAR. This larger reduction with respect to BIPOLAR might be due to the fact that, in addition to CG-

nulling, BIPOLAR waveforms achieve eddy current-nulling for some decay constant (32) which might require higher TEs for a given b-value.

This work has several limitations. ODGD waveforms were applied to the spin-echo diffusion pulse sequence, and validated on phantom experiments and 10 healthy volunteers. Future validation in a larger cohort including patients is still needed. However, TE-related SNR gains, as well as CG-effects are largely subject-independent, so these results are likely generalizable. Further, in this work the computation of ODGD waveforms was performed offline (with relatively long computation times between 2 and 8 min) and then loaded on the scanner. Next steps will include accelerated computation to achieve finer time resolution with reasonable computation times, and online implementation of ODGD waveforms for better sequence design flexibility. In addition, comparing different motion-compensated waveforms in liver acquisitions is challenging as shown in Figure 6. Different TEs might lead to different T_2 shine-through and SNR. Further, not using cardiac gating might produce slight mis-registrations across b-values and across multiple averages. Finally, rapidly moving blood spins might also result in different signal behavior under different diffusion-weighting gradient waveforms, which might in turn lead to different ADC values in/near blood vessels.

Future work includes further validation in brain, liver, and heart, in volunteers and patients. Additionally, several extensions of the proposed formulation are desirable. Minimization of peripheral nerve stimulation effects may be included, as shown in Ref. (33). Further, prospective and retrospective techniques may be used to diminish eddy current induced distortions (34), although it is also possible to extend the ODGD formulation to reduce the eddy current distortions as recently proposed in Ref. (21). Future work may extend the ODGD formulation beyond the spin-echo sequence to, for example, the gradient echo, stimulated echo or twice refocused spin-echo (TRSE) diffusion sequences. Specifically, application of ODGD-CG to TRSE may reduce the strong phase accrual suffered by TRSE from CG-effects (9), while minimizing EC-induced distortions.

CONCLUSIONS

We have proposed a novel method, termed ODGD, to design motion-compensated and CG-nulling diffusion-weighting gradient waveforms that optimize the TE for a given b-value. Theoretical results, simulations, as well as experiments in phantoms and healthy volunteers, demonstrated that ODGD motion-compensated diffusion-weighting gradient waveforms resulted in reduced TEs, increased SNR, increased motion robustnes, and reduced ADC bias compared to the state-of-the-art.

ACKNOWLEDGMENTS

The authors acknowledge grant TEC2013-44194-P and VA069U16 from Ministerio de Economía y Competitividad of Spain, and Junta de Castilla y León, respectively. In addition, the authors acknowledge the Consejería de Educación of Junta de Castilla y León and the Fondo Social Europeo. The authors also thank the National Institutes of Health, NIDDK Wisconsin Multidisciplinary K12 Urologic Research Career Development Program K12DK100022 (PD: D. Bjorling). Finally, the authors would like to acknowledge research support from GE Healthcare.

References

1. Taouli B, Koh DM. Diffusion-weighted MR imaging of the liver 1. Radiology 2009;254:47–66.

2. Koh DM, Collins DJ. Diffusion-weighted MRI in the body: applications and challenges in oncology. American Journal of Roentgenology 2007;188:1622–1635.

3. Stejskal EO, Tanner JE. Spin diffusion measurements: spin echoes in the presence of a time-dependent field gradient. The journal of chemical physics 1965;42:288–292.

4. Padhani AR, Liu G, Mu-Koh D, Chenevert TL, Thoeny HC, Takahara T, Dzik-Jurasz A, Ross BD, Van Cauteren M, Collins D, et al. Diffusion-weighted magnetic resonance imaging as a cancer biomarker: consensus and recommendations. Neoplasia 2009;11:102–125.

5. Le Bihan D, Breton E, Lallemand D, Grenier P, Cabanis E, Laval-Jeantet M. MR imaging of intravoxel incoherent motions: application to diffusion and perfusion in neurologic disorders. Radiology 1986;161:401–407.

6. Murtz P, Flacke S, Traber F, van den Brink JS, Gieseke J, Schild HH. Abdomen: diffusion-weighted MR imaging with pulse-triggered single-shot sequences. Radiology 2002;224:258–264.

7. Liau J, Lee J, Schroeder ME, Sirlin CB, Bydder M. Cardiac motion in diffusion-weighted MRI of the liver: artifact and a method of correction. Journal of Magnetic Resonance Imaging 2012; 35:318–327.

8. Bernstein MA, Zhou XJ, Polzin JA, King KF, Ganin A, Pelc NJ, Glover GH. Concomitant gradient terms in phase contrast MR: analysis and correction. Magnetic resonance in medicine 1998;39:300–308.

9. Baron C, Lebel R, Wilman A, Beaulieu C. The effect of concomitant gradient fields on diffusion tensor imaging. Magnetic resonance in medicine 2012;68:1190–1201.

10. Meier C, Zwanger M, Feiweier T, Porter D. Concomitant field terms for asymmetric gradient coils: Consequences for diffusion, flow, and echo-planar imaging. Magnetic resonance in medicine 2008;60:128–134.

11. Anderson AW, Gore JC. Analysis and correction of motion artifacts in diffusion weighted imaging. Magnetic resonance in medicine 1994;32:379–387.

12. Trouard TP, Sabharwal Y, Altbach MI, Gmitro AF. Analysis and comparison of motion-correction techniques in diffusion-weighted imaging. Journal of Magnetic Resonance Imaging 1996;6:925–935.

13. Norris DG. Implications of bulk motion for diffusion-weighted imaging experiments: Effects, mechanisms, and solutions. Journal of magnetic resonance imaging 2001;13:486–495.

14. Murphy P, Wolfson T, Gamst A, Sirlin C, Bydder M. Error model for reduction of cardiac and respiratory motion effects in quantitative liver DW-MRI. Magnetic resonance in medicine 2013;70:1460–1469.

15. Simonetti OP, Wendt RE, Duerk JL. Significance of the point of expansion in interpretation of gradient moments and motion sensitivity. Journal of Magnetic Resonance Imaging 1991; 1:569–577.

16. Ozaki M, Inoue Y, Miyati T, Hata H, Mizukami S, Komi S, Matsunaga K, Woodhams R. Motion artifact reduction of diffusion-weighted MRI of the liver: Use of velocity-compensated diffusion gradients combined with tetrahedral gradients. Journal of Magnetic Resonance Imaging 2013; 37:172–178.

17. Stoeck CT, Von Deuster C, Genet M, Atkinson D, Kozerke S. Second-order motion-compensated spin echo diffusion tensor imaging of the human heart. Magnetic resonance in medicine 2016;75:1669–1676.

18. Norris DG, Hutchison JM. Concomitant magnetic field gradients and their effects on imaging at low magnetic field strengths. Magnetic resonance imaging 1990;8:33–37.

19. Sica CT, Meyer CH. Concomitant gradient field effects in balanced steady-state free precession. Magnetic resonance in medicine 2007;57:721–730.

20. Zhou XJ, Tan SG, Bernstein MA. Artifacts induced by concomitant magnetic field in fast spin-echo imaging. Magnetic resonance in medicine 1998;40:582–591.

21. Aliotta E, Wu HH, Ennis DB. Convex optimized diffusion encoding (CODE) gradient waveforms for minimum echo time and bulk motion–compensated diffusion-weighted MRI. Magnetic resonance in medicine 2017;77:717–729.

22. Welsh CL, DiBella EV, Hsu EW. Higher-order motion-compensation for in vivo cardiac diffusion tensor imaging in rats. IEEE transactions on medical imaging 2015;34:1843–1853.

23. Wang X, Reeder SB, Hernando D. An acetone-based phantom for quantitative diffusion MRI. Journal of Magnetic Resonance Imaging 2017;.

24. Aja-Fernández S, Vegas-Sánchez-Ferrero G. Statistical Analysis of Noise in MRI. Modeling, Filtering and Estimation. Springer International Publishing 2016.

25. DeVore MD, Lanterman AD, O Sullivan JA. ATR performance of a Rician model for SAR images. In Proceedings of the SPIE - The International Society for Optical Engineering. International Society for Optical Engineering; 1999 2000; pp. 34–47.

26. Aja-Fernández S, Pie T, Vegas-Sánchez-Ferrero G, et al. Spatially variant noise estimation in MRI: A homomorphic approach. Medical image analysis 2015;20:184–197.

27. Hamilton G, Middleton MS, Hooker JC, Haufe WM, Forbang NI, Allison MA, Loomba R, Sirlin CB. In vivo breath-hold 1H MRS simultaneous estimation of liver proton density fat fraction, and T1 and T2 of water and fat, with a multi-TR, multi-TE sequence. Journal of Magnetic Resonance Imaging 2015;42:1538–1543.

28. Imaging B. 150028 USA Instruments INC. SNR Phantom for GE MRI. `https://parts.blockimaging.com/150028-USA-Instruments--INC.-SNR-Phantom-for-GE-MRI-for-GE--Closed-MRI/`. [Online; accessed 07-January-2018].

29. Sijbers J, den Dekker AJ, Scheunders P, Van Dyck D. Maximum-likelihood estimation of Rician distribution parameters. IEEE Transactions on Medical Imaging 1998;17:357–361.

30. Holz M, Heil SR, Sacco A. Temperature-dependent self-diffusion coefficients of water and six selected molecular liquids for calibration in accurate 1H NMR PFG measurements. Physical Chemistry Chemical Physics 2000;2:4740–4742.

31. Butts K, Riederer SJ, Ehman RL, Thompson RM, Jack CR. Interleaved echo planar imaging on a standard MRI system. Magnetic resonance in medicine 1994;31:67–72.

32. Alexander AL, Tsuruda JS, Parker DL. Elimination of eddy current artifacts in diffusion-weighted echo-planar images: the use of bipolar gradients. Magnetic Resonance in Medicine 1997;38:1016–1021.

33. Schulte RF, Noeske R. Peripheral nerve stimulation-optimal gradient waveform design. Magnetic resonance in medicine 2015;74:518–522.

34. Xu D, Maier JK, King KF, Collick BD, Wu G, Peters RD, Hinks RS. Prospective and retrospective high order eddy current mitigation for diffusion weighted echo planar imaging. Magnetic resonance in medicine 2013;70:1293–1305.

Figure captions

Figure 1: Traditional waveforms (a), Convex Optimized Diffusion Encoding (CODE) gradient waveforms (b), and Optimized Diffusion-weighting Gradient waveform Designs (ODGD) without (c) and with (d) concomitant gradients (CGs) nulling for b = 1000 s/mm^2 and T_{EPI} = 26.4 ms. CODE and ODGD waveforms without and with CG-nulling reduced the TE of the traditional waveforms (MONO, BIPOLAR, and MOCO) in all cases. These traditional waveforms have equivalent or symmetric shapes before and after the refocusing pulse, and therefore lead to dead times between the radiofrequency pulses (due to the need for additional time for the EPI readout between the end of the diffusion waveform and the echo time). In contrast, the CODE framework and the ODGD formulation seek to use the available time optimally in order to minimize the TE.

Figure 2: Minimum TE achieved for the range of b-values 100 - 2000 s/mm^2 and T_{EPI} (EPI readout time to the center of k-space) of 26.4 ms for ODGD-M_n, CODE-M_n, and the traditional waveforms (MONO, BIPOLAR, and MOCO) for different moment constraints, M_0, M_1, and M_2, respectively (a). TE reduction (ΔTE) achieved using ODGD-M_n compared to CODE-M_n for the same range of b-values and T_{EPI} in the range of 15 - 50 ms (b). There is no TE reduction (ΔTE = 0) for zeroth-order moment-nulling (M_0), but there is TE reduction for first- and second-order moment-nulling (M_1 and M_2, respectively). The TE reduction is greater for higher b-values, longer T_{EPI}, and higher-order moment-nulling.

Figure 3: Minimum TE achieved for a range of b-values 100 - 2000 s/mm^2 and T_{EPI} (EPI readout time to the center of k-space) of 26.4 ms for ODGD-M_n-CG and the traditional waveforms (MONO, BIPOLAR, and MOCO) for different moment constraints, M_0, M_1, and M_2, respectively (a). TE reduction (ΔTE) achieved using ODGD-M_n-CG compared to the traditional waveforms for the same range of b-values and T_{EPI} in the range of 15 - 50 ms (b). ΔTE is larger for higher b-values and T_{EPI}, and larger for the M_1 constraint than for M_0, or M_2.

Figure 4: Diffusion-weighted images of the acetone phantom experiments acquired with CODE-M_2 and ODGD-M_2 at b-value 1000 s/mm^2 (a). SNR of the same images (b). Top row of the set of 10 vials have short $T_2 \approx 39.5$ ms (vial numbers 1, 3, 5, 7, 9), and bottom row have long $T_2 \approx 83.5$ ms (vial numbers 2, 4, 6, 8, 10). Distribution of the SNR values of each vial grouped by $T_2 \approx 39.5$ ms (c), and $T_2 \approx 83.5$ ms (d). From left to right, distributions are ordered as vials in (a). Red boxes show the distribution of CODE-M_2 and black boxes the distribution of ODGD-M_2. There is a statistically significant ($P < 0.05$) SNR increase for every vial of ODGD-M_2 compared to

CODE-M_2 except for vials with ADC = 1.9×10^{-3} mm^2/s.

Figure 5: Axial trace diffusion-weighted images (DWI) acquired at 4.5 cm from isocenter of a representative brain are shown acquired with BIPOLAR, ODGD-M_1, and ODGD-M_1-CG with a b-value of 100 s/mm^2 (a). Corresponding average trace ADC map of the BIPOLAR acquisition (b). ODGD-M_1 and ODGD-M_1-CG average trace ADC maps pixelwise subtracted with the BIPOLAR average trace ADC map (c). Mean ± 95% CI SNR values of the trace DW images (d), and average trace ADC values (e) across ROIs set on white matter of the 10 volunteers. ODGD-M_1 leads to higher statistically significant SNR than BIPOLAR and ODGD-M_1-CG, $P < 1$ x 10^{-6} and $P < 0.05$, respectively. ODGD-M_1-CG also leads to statistically significant higher SNR than BIPOLAR with $P < 0.005$. ODGD-M_1 average trace ADC map is positively biased ($P < 0.005$) with respect to BIPOLAR. There is no statistically significant difference between the average trace ADC maps of ODGD-M_1-CG and BIPOLAR.

Figure 6: Axial diffusion-weighted images of a representative liver are shown acquired with MONO, CODE-M_2, and ODGD-M_2 with a b-value of 500 s/mm^2 (a). Corresponding ADC maps (b). MONO ADC maps have heterogeneous positive bias throughout the liver due to intravoxel signal dephasing at b-value of 500 s/mm^2 produced by bulk motion. ODGD-M_2 and CODE-M_2 waveforms achieve more spatially homogeneous DW images and ADC maps than MONO, showing better motion robustness. ADC values on a ROI on segment II of the liver (blue ROI) of a representative volunteer are 2.46±0.38 × 10^{-3} mm^2/s for MONO, 1.85±0.2 × 10^{-3} mm^2/s for CODE-M_2, and 1.53±0.21 × 10^{-3} mm^2/s for ODGD-M_2.

Figure 7: Axial diffusion-weighted images of the liver are shown acquired with MOCO, CODE-M_2, ODGD-M_2, and ODGD-M_2-CG with a b-value of 100 s/mm^2 (a). Signal-to-noise ratio (SNR) maps of these acquisitions (smoothed with an average filter for better representation) (b). Liver SNR measurements in the 10 volunteers, for each of the diffusion waveforms (c). ODGD-M_2 and ODGD-M_2-CG lead to statistically significant ($P < 0.05$) higher SNR than MOCO and CODE-M_2. There is no statistically significant difference between ODGD-M_2 and ODGD-M_2-CG.

Figure 8: k-Space of the water phantom experiments of slices at isocenter (0 cm) and 4.5 cm from isocenter with MONO, ODGD-M_0, and ODGD-M_0-CG, b-value of 1000 s/mm^2, and diffusion-weighting direction D_{xyz}, (a) and (b), respectively. FWHMy indicates the full-width-half-maximum along the phase-encoding direction (y-axes). ODGD-M_0 shows broader FWHMy than MONO and ODGD-M_0-CG, and k-space shifting towards the upper left corner at 4.5 cm from isocenter. MONO and ODGD-M_0-CG show little blurring and no k-space shifting.

Figure 9: Measured ADC maps along each gradient direction combination (D_n) of the water phantom experiment with the BIPOLAR waveform (a). Measured ADC maps of the simulated acquisition of the water phantom experiment for ODGD-M_1 (b). Measured ADC maps of the waveforms ODGD-M_1 (c) and ODGD-M_1-CG (d). The reference ADC value of 1.98×10^{-3} mm^2/s, dotted line, was measured as the average of D_x, D_y and D_z of the BIPOLAR acquisition. Acquisitions with BIPOLAR and ODGD-M_1-CG waveforms considerably reduced the bias of the ADC maps introduced by the concomitant gradients.

Table 1: Optimized Diffusion-weighted Gradient waveform Design (ODGD) formulation.

	ODGD Formulation		
Pulse Sequence Constraints	$G(\mathrm{RF}_{90}) = 0$	$G(\mathrm{RF}_{180}) = 0$	$G(\mathrm{T}_{\mathrm{EPI}}) = 0$
Hardware Constraints	$G(t) \leq \mathrm{G}_{\mathrm{Max}}$	$\dot{G}(t) \leq \mathrm{SR}_{\mathrm{Max}}$	
Moment Constraint	$M_{\mathrm{n}} = \gamma \int_0^{T_{\mathrm{Diff}}} t^{\mathrm{n}} G(t) dt = 0 \quad \text{where} \quad \mathrm{n} = 0, 1, 2...$		
Concomitant Gradients Constraint	$\phi_c(x, y, z) = \gamma \int_0^{T_{\mathrm{Diff}}} B_c(x, y, z, t) dt = 0$		
b-value Formulation	$b = \gamma^2 \int_0^{T_{\mathrm{Diff}}} F(t)^2 dt$	$F(t) = \int_0^t G(\tau) d\tau$	
Objective Function	${}^a G(t) = \arg\max_G b(G)$		

[a] G(t) is the diffusion-weighting gradient waveform.

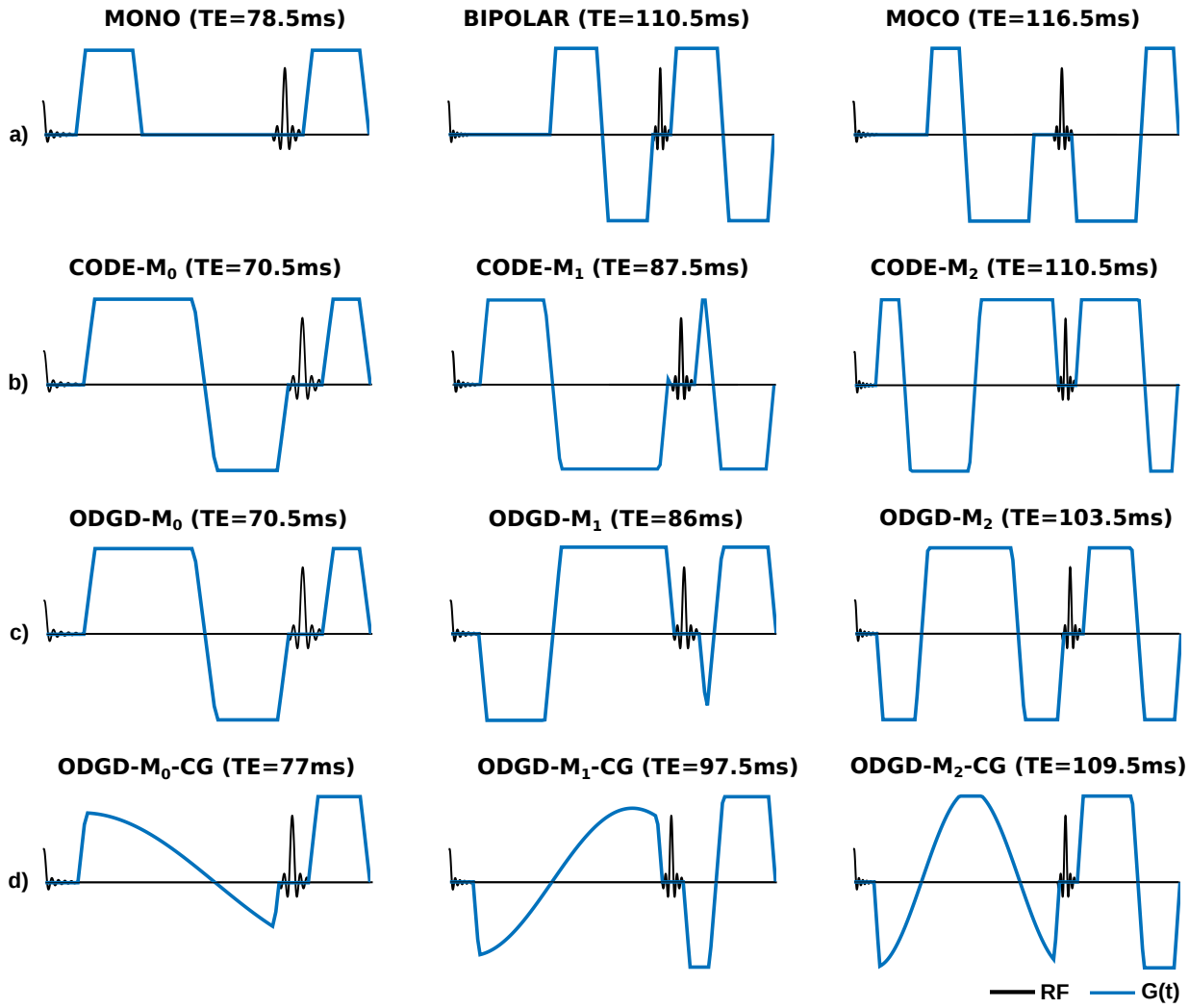

Figure 1: Traditional waveforms (a), Convex Optimized Diffusion Encoding (CODE) gradient waveforms (b), and Optimized Diffusion-weighting Gradient waveform Designs (ODGD) without (c) and with (d) concomitant gradients (CGs) nulling for b = 1000 s/mm^2 and T_{EPI} = 26.4 ms. CODE and ODGD waveforms without and with CG-nulling reduced the TE of the traditional waveforms (MONO, BIPOLAR, and MOCO) in all cases. These traditional waveforms have equivalent or symmetric shapes before and after the refocusing pulse, and therefore lead to dead times between the radiofrequency pulses (due to the need for additional time for the EPI readout between the end of the diffusion waveform and the echo time). In contrast, the CODE framework and the ODGD formulation seek to use the available time optimally in order to minimize the TE.

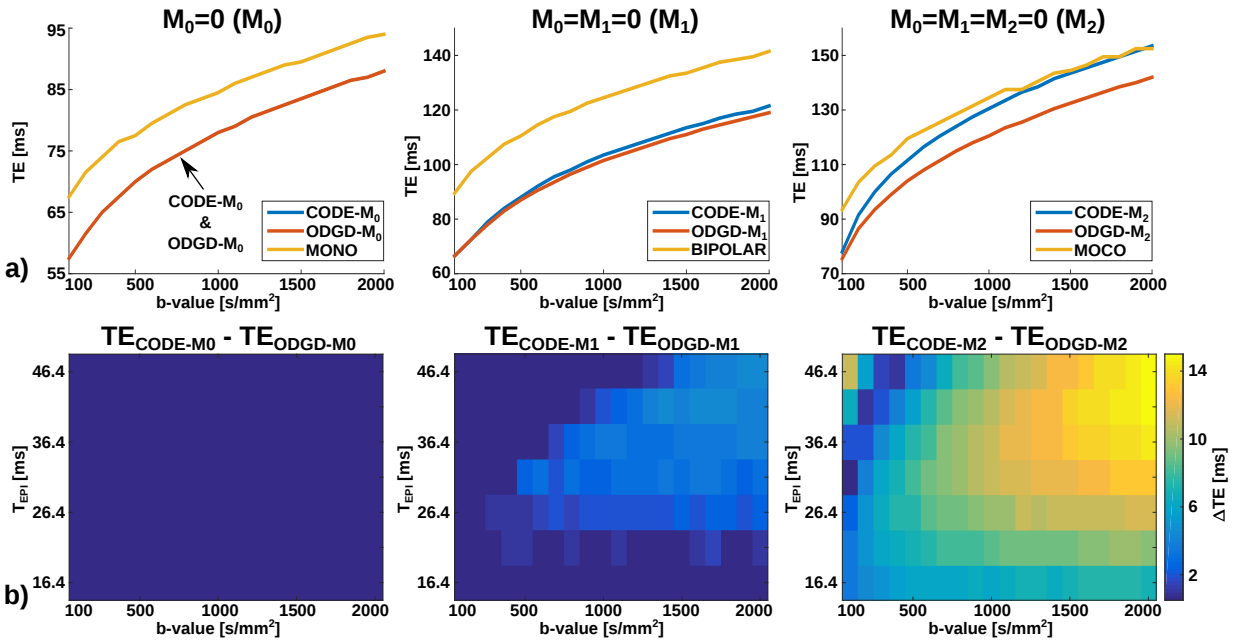

Figure 2: Minimum TE achieved for the range of b-values 100 - 2000 s/mm^2 and T_{EPI} (EPI readout time to the center of k-space) of 26.4 ms for ODGD-M_n, CODE-M_n, and the traditional waveforms (MONO, BIPOLAR, and MOCO) for different moment constraints, M_0, M_1, and M_2, respectively (a). TE reduction (ΔTE) achieved using ODGD-M_n compared to CODE-M_n for the same range of b-values and T_{EPI} in the range of 15 - 50 ms (b). There is no TE reduction ($\Delta TE = 0$) for zeroth-order moment-nulling (M_0), but there is TE reduction for first- and second-order moment-nulling (M_1 and M_2, respectively). The TE reduction is greater for higher b-values, longer T_{EPI}, and higher-order moment-nulling.

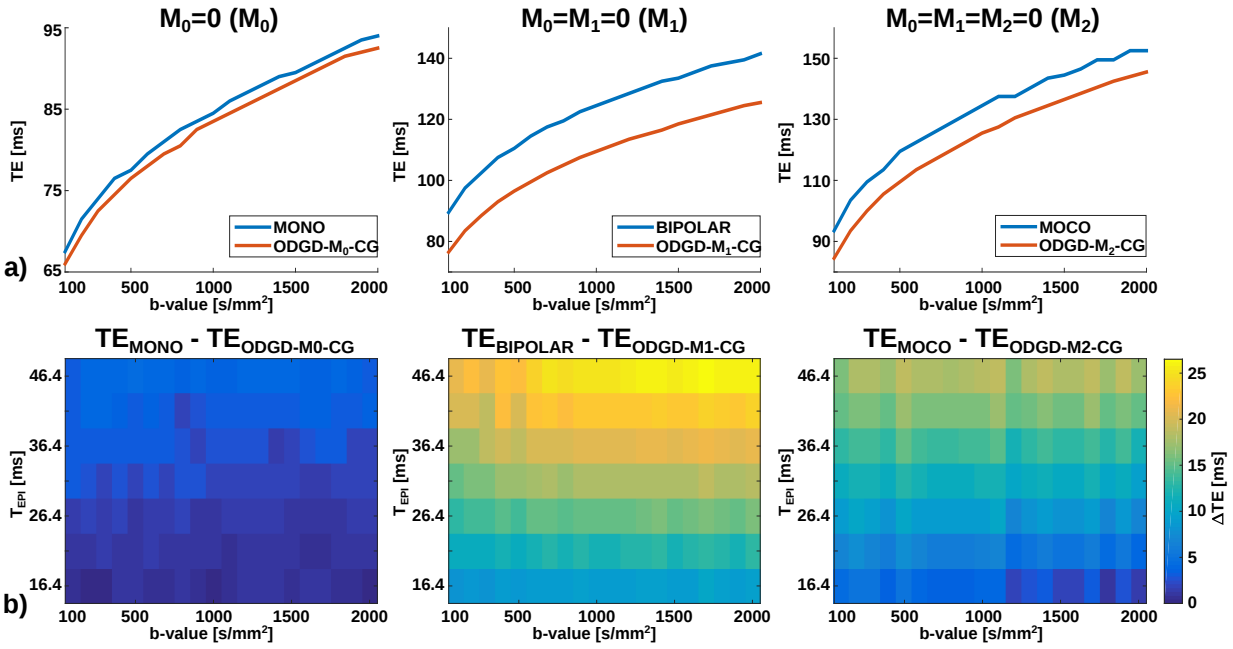

Figure 3: Minimum TE achieved for a range of b-values 100 - 2000 s/mm^2 and T_{EPI} (EPI readout time to the center of k-space) of 26.4 ms for ODGD-M_n-CG and the traditional waveforms (MONO, BIPOLAR, and MOCO) for different moment constraints, M_0, M_1, and M_2, respectively (a). TE reduction (ΔTE) achieved using ODGD-M_n-CG compared to the traditional waveforms for the same range of b-values and T_{EPI} in the range of 15 - 50 ms (b). ΔTE is larger for higher b-values and T_{EPI}, and larger for the M_1 constraint than for M_0, or M_2.

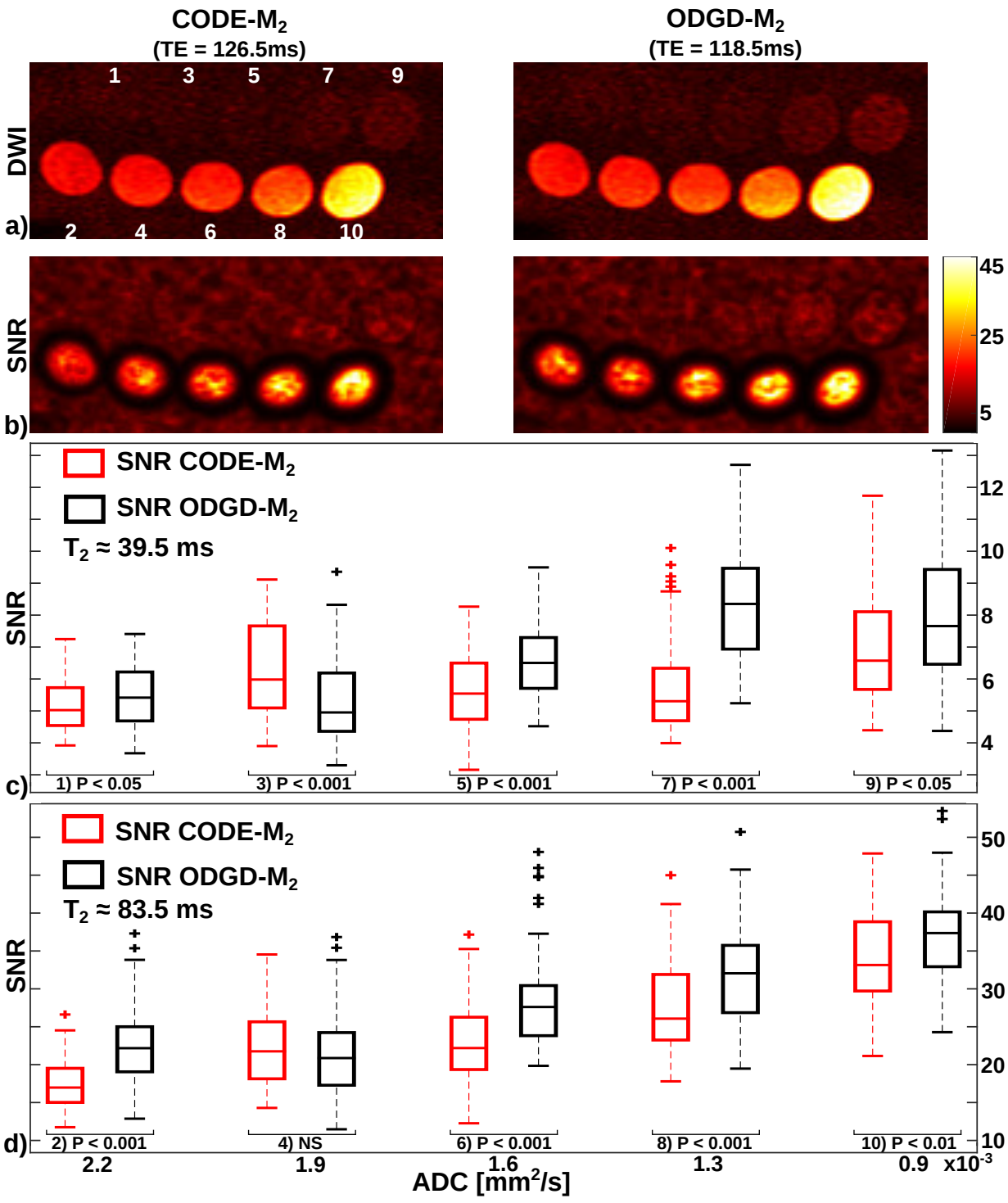

Figure 4: Diffusion-weighted images of the acetone phantom experiments acquired with CODE-M_2 and ODGD-M_2 at b-value 1000 s/mm^2 (a). SNR of the same images (b). Top row of the set of 10 vials have short $T_2 \approx 39.5$ ms (vial numbers 1, 3, 5, 7, 9), and bottom row have long $T_2 \approx 83.5$ ms (vial numbers 2, 4, 6, 8, 10). Distribution of the SNR values of each vial grouped by $T_2 \approx 39.5$ ms (c), and $T_2 \approx 83.5$ ms (d). From left to right, distributions are ordered as vials in (a). Red boxes show the distribution of CODE-M_2 and black boxes the distribution of ODGD-M_2. There is a statistically significant ($P < 0.05$) SNR increase for every vial of ODGD-M_2 compared to CODE-M_2 except for vials with ADC = 1.9×10^{-3} mm^2/s.

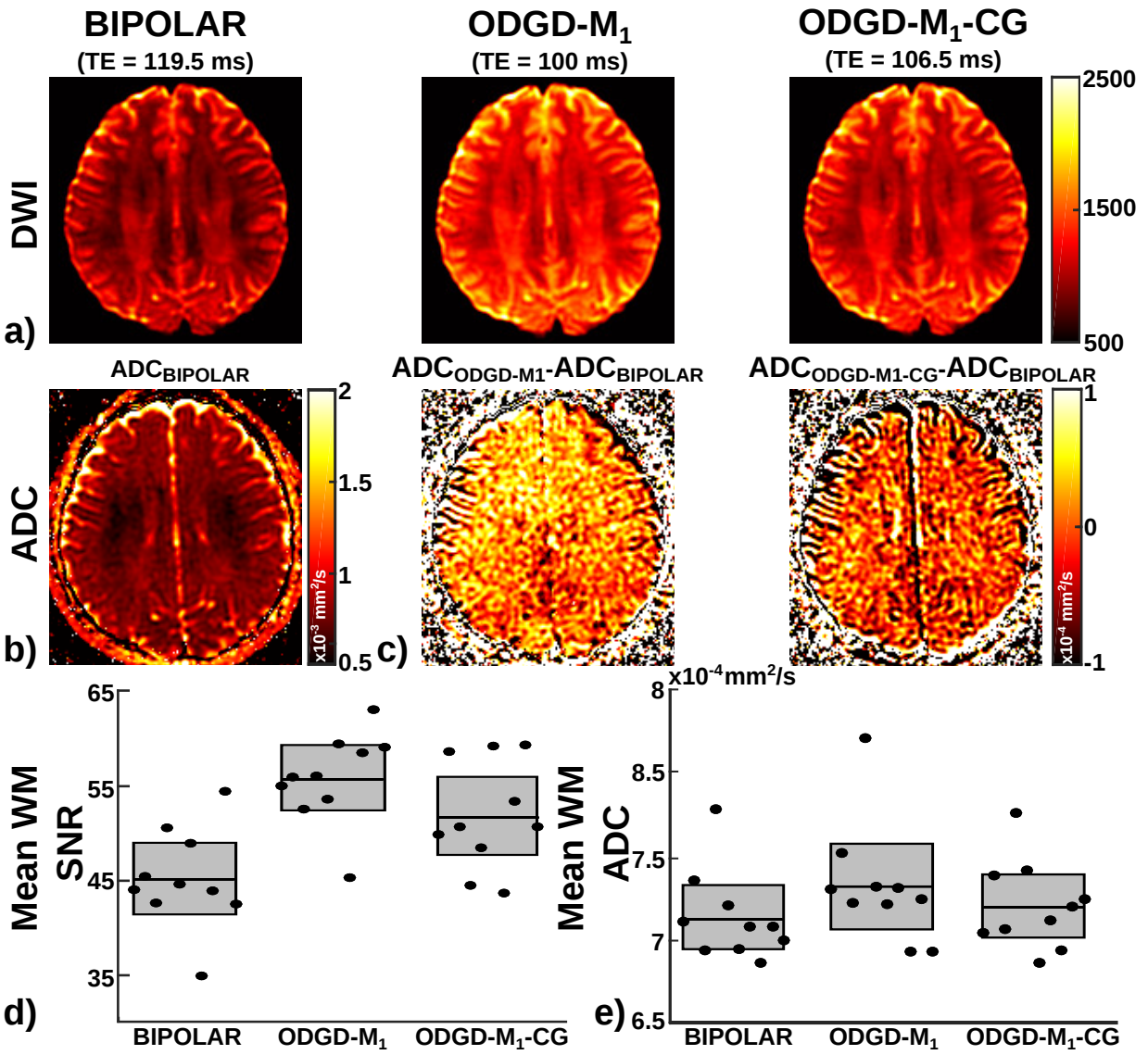

Figure 5: Axial trace diffusion-weighted images (DWI) acquired at 4.5 cm from isocenter of a representative brain are shown acquired with BIPOLAR, ODGD-M_1, and ODGD-M_1-CG with a b-value of 100 s/mm^2 (a). Corresponding average trace ADC map of the BIPOLAR acquisition (b). ODGD-M_1 and ODGD-M_1-CG average trace ADC maps pixelwise subtracted with the BIPOLAR average trace ADC map (c). Mean $\pm$ 95% CI SNR values of the trace DW images (d), and average trace ADC values (e) across ROIs set on white matter of the 10 volunteers. ODGD-M_1 leads to higher statistically significant SNR than BIPOLAR and ODGD-M_1-CG, $P < 1 \times 10^{-6}$ and $P < 0.05$, respectively. ODGD-M_1-CG also leads to statistically significant higher SNR than BIPOLAR with $P < 0.005$. ODGD-M_1 average trace ADC map is positively biased ($P < 0.005$) with respect to BIPOLAR. There is no statistically significant difference between the average trace ADC maps of ODGD-M_1-CG and BIPOLAR.

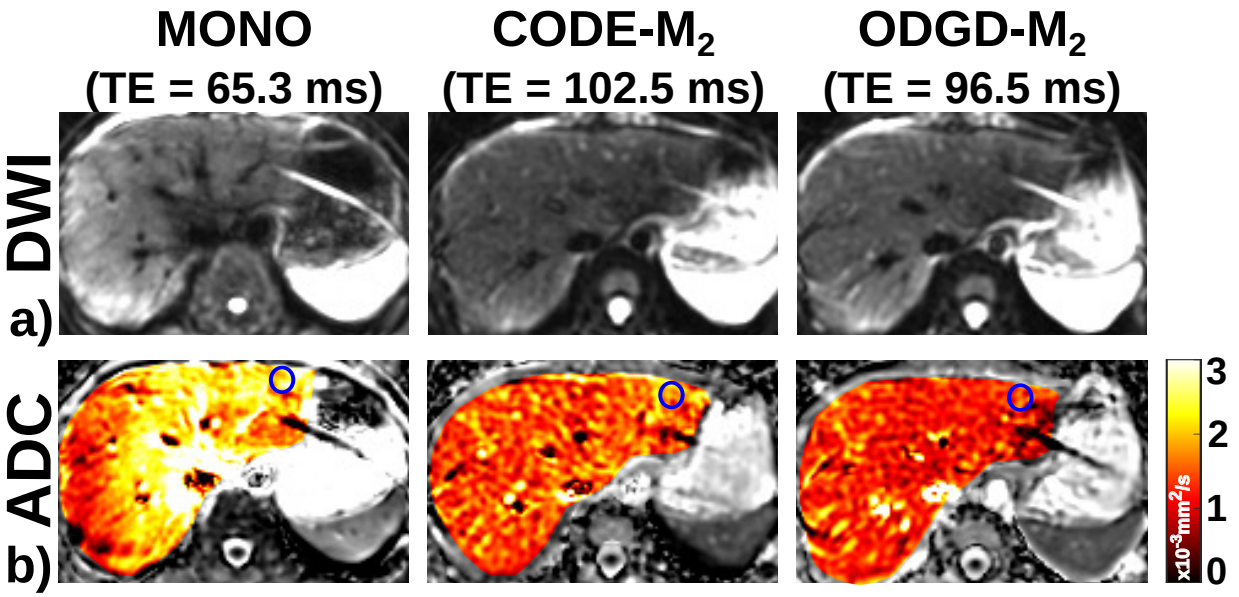

Figure 6: Axial diffusion-weighted images of a representative liver are shown acquired with MONO, CODE-M_2, and ODGD-M_2 with a b-value of 500 s/mm^2 (a). Corresponding ADC maps (b). MONO ADC maps have heterogeneous positive bias throughout the liver due to intravoxel signal dephasing at b-value of 500 s/mm^2 produced by bulk motion. ODGD-M_2 and CODE-M_2 waveforms achieve more spatially homogeneous DW images and ADC maps than MONO, showing better motion robustness. ADC values on a ROI on segment II of the liver (blue ROI) of a representative volunteer are 2.46$\pm$0.38 $\times$ 10^{-3} mm^2/s for MONO, 1.85$\pm$0.2 $\times$ 10^{-3} mm^2/s for CODE-M_2, and 1.53$\pm$0.21 $\times$ 10^{-3} mm^2/s for ODGD-M_2.

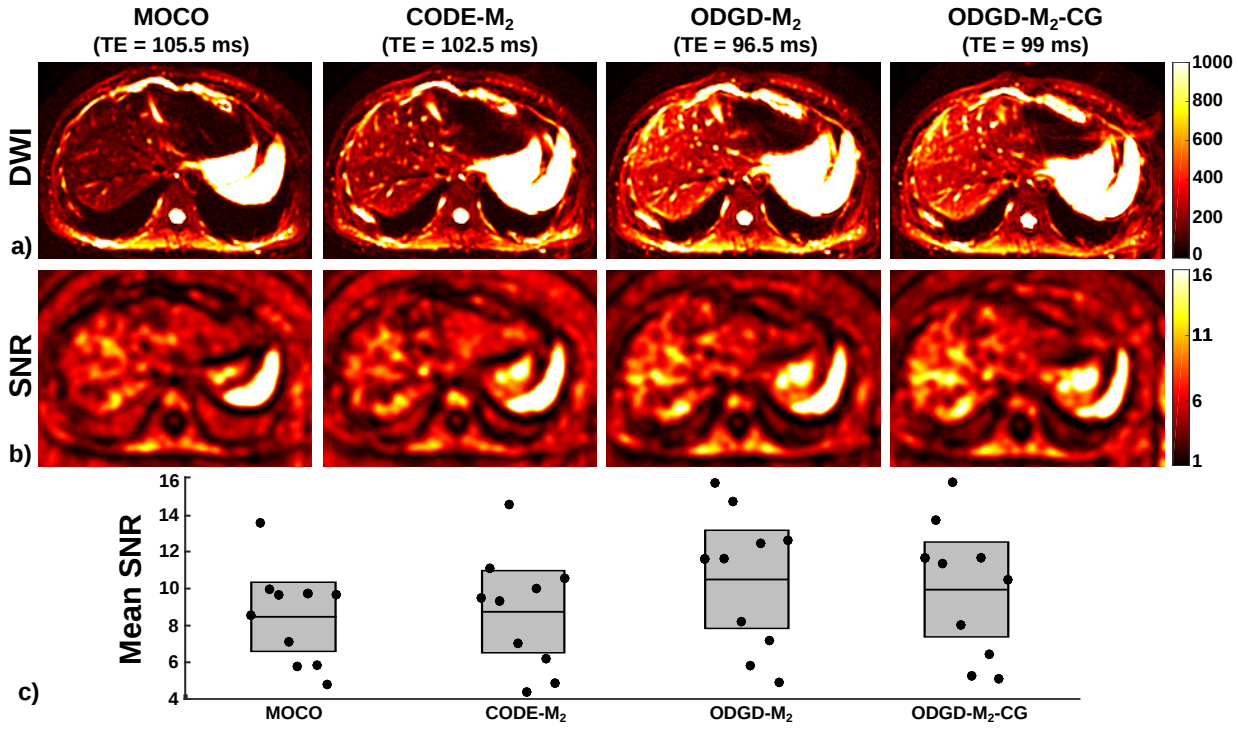

Figure 7: Axial diffusion-weighted images of the liver are shown acquired with MOCO, CODE-M_2, ODGD-M_2, and ODGD-M_2-CG with a b-value of 100 s/mm^2 (a). Signal-to-noise ratio (SNR) maps of these acquisitions (smoothed with an average filter for better representation) (b). Liver SNR measurements in the 10 volunteers, for each of the diffusion waveforms (c). ODGD-M_2 and ODGD-M_2-CG lead to statistically significant ($P < 0.05$) higher SNR than MOCO and CODE-M_2. There is no statistically significant difference between ODGD-M_2 and ODGD-M_2-CG.

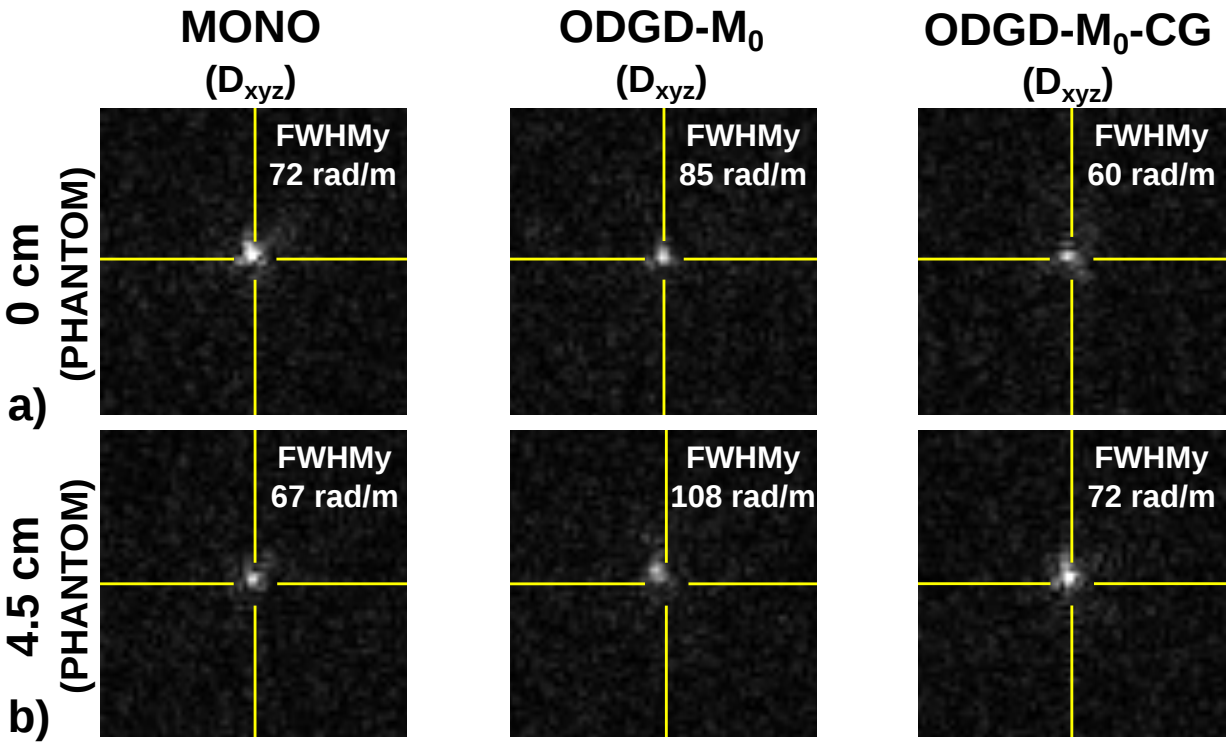

Figure 8: k-Space of the water phantom experiments of slices at isocenter (0 cm) and 4.5 cm from isocenter with MONO, ODGD-M_0, and ODGD-M_0-CG, b-value of 1000 s/mm^2, and diffusion-weighting direction D_{xyz}, (a) and (b), respectively. FWHMy indicates the full-width-half-maximum along the phase-encoding direction (y-axes). ODGD-M_0 shows broader FWHMy than MONO and ODGD-M_0-CG, and k-space shifting towards the upper left corner at 4.5 cm from isocenter. MONO and ODGD-M_0-CG show little blurring and no k-space shifting.

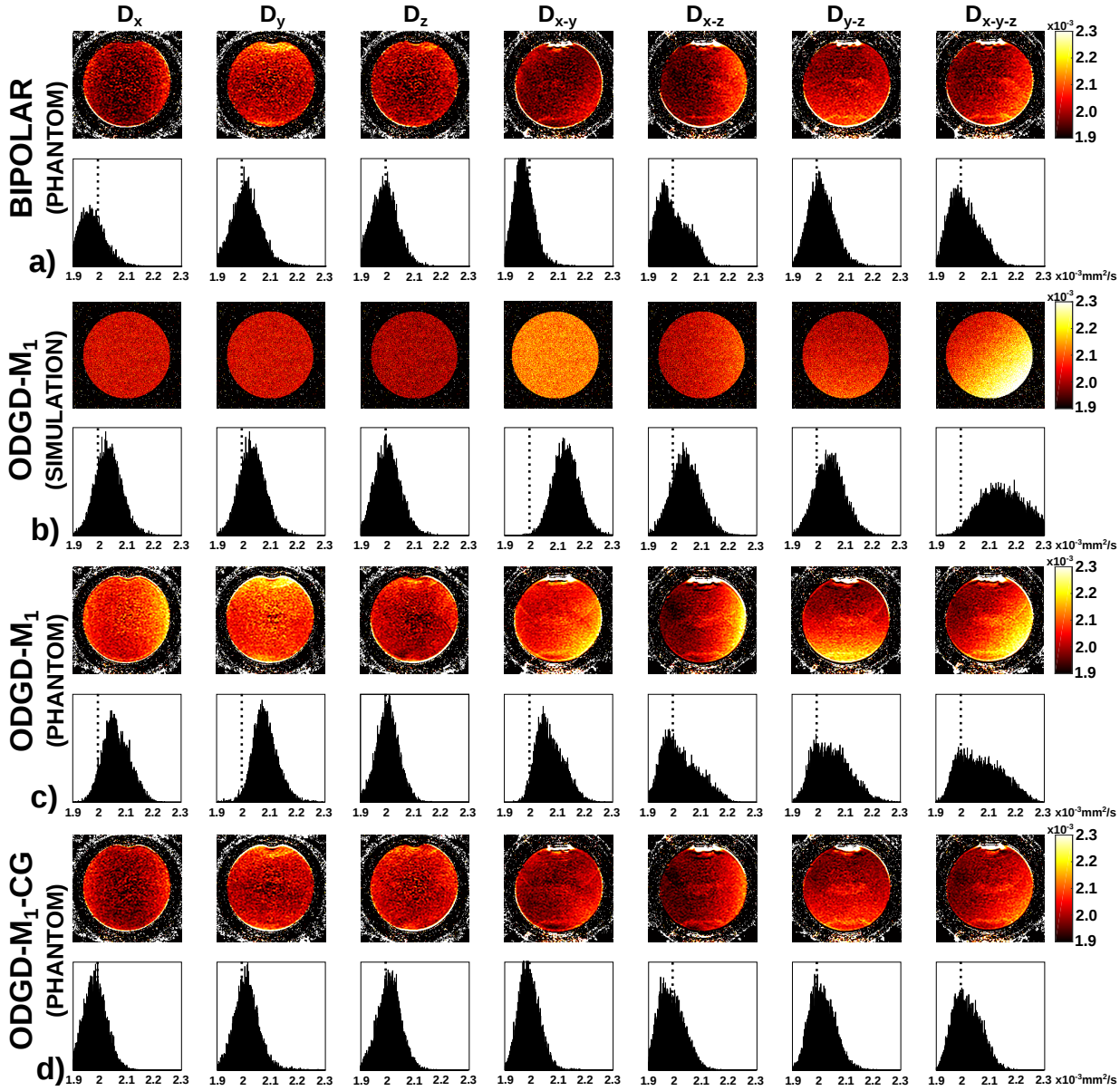

Figure 9: Measured ADC maps along each gradient direction combination (D_n) of the water phantom experiment with the BIPOLAR waveform (a). Measured ADC maps of the simulated acquisition of the water phantom experiment for ODGD-M_1 (b). Measured ADC maps of the waveforms ODGD-M_1 (c) and ODGD-M_1-CG (d). The reference ADC value of 1.98×10^{-3} mm^2/s, dotted line, was measured as the average of D_x, D_y and D_z of the BIPOLAR acquisition. Acquisitions with BIPOLAR and ODGD-M_1-CG waveforms considerably reduced the bias of the ADC maps introduced by the concomitant gradients.